Journal of Power Sources 185 (2008) 261–271

Contents lists available at ScienceDirect

Journal of Power Sources

journal homepage: www.elsevier.com/locate/jpowsour

Modeling of two-phase transport in the diffusion media of polymer electrolyte fuel cells

Yun Wang*

Renewable Energy Resources Lab (RERL) and National Fuel Cell Research Center, Department of Mechanical and Aerospace Engineering, The University of California, Irvine, Irvine, CA 92697-3975, USA

ARTICLE INFO

Article history:
Received 29 May 2008
Received in revised form 3 July 2008
Accepted 4 July 2008
Available online 17 July 2008

Keywords:
Polymer electrolyte fuel cell
Two-phase modeling
Numerical simulation
Multiphase flow
Anode flooding

ABSTRACT

A three-dimensional model of polymer electrolyte fuel cells (PEFCs) is developed to investigate multiphase flows, species transport, and electrochemical processes in fuel cells and their interactions. This two-phase model consists of conservation principles of mass, momentum, species concentration and charges, and elucidates the key physicochemical mechanisms in the constituent components of PEFCs that govern cell performance. Efforts are made to formulate two-phase transport in the anode diffusion media and its coupling with cathode flooding as well as the interaction between single- and two-phase flows. Numerical simulations are carried out to investigate multiphase flow, electrochemical activity, and transport phenomena and the intrinsic couplings of these processes inside a fuel cell at low humidity. The results indicate that multiphase flows may exist in both anode and cathode diffusion media at low-humidity operation, and two-phase flow emerges near the outlet for co-flow configuration while is present in the middle of the fuel cell for counter-flow one. The validated numerical tools can be applied to investigate vital issues related to anode performance and degradation arising from flooding for PEFCs.

Published by Elsevier B.V.

1. Introduction

Fuel cells, converting the chemical energy stored in fuels directly and efficiently to electricity via electrochemical reactions, have become the focus of new energy development due to their noteworthy features of high efficiency and low emissions [1–3]. Among all types of fuel cells, the polymer electrolyte fuel cells (PEFCs), also called polymer electrolyte membrane (PEM) fuel cells, have captured the public attention for both mobile and portable applications [4,5]. In addition to providing high power density, PEFCs work at low temperature (typically <100 °C), only produce water as byproduct and can be compactly assembled. These factors make them one of the premiere candidates as the next generation power generator.

Fig. 1 schematically shows a single PEFC. A typical PEFC consists of the following components: bipolar plates with flow channels grooved in, gas diffusion media (DMs), and a proton-conductive membrane with platinum catalyst coated on each side. The bipolar plates, usually graphite or metal plates, play important roles of electronically connecting the adjacent cells and distributing the reactant gases over the anode and cathode. Gas diffusion media are usually carbon-based substrates such as carbon paper and cloth [6,7], see Fig. 2, which are placed on the membrane electrode assembly (MEA) and perform multiple functions: passages for species and heat transport and electronic connection between the bipolar plates and catalyst layers. Important constituent phases of the catalyst layer include C/Pt or Pt alloy catalyst, ionomer, and void space. The electrochemical reactions take place at the triple-phase boundary (TPB) of the catalyst layer. The proton-conducting membrane, typically made of Nafion®, plays dual roles as the gas separator and electrolyte. The molecule of Nafion® is characterized by hydrophobic, fluorinated main chains with hydrophilic sulfonic acid groups, allowing protons to weakly attract to the SO_3^- and travel in hydrated region.

Mathematical modeling of PEFCs has been a rapidly growing field of research. Early models mostly focus on electrochemical modeling in one or pseudo-two dimensions and deal with single-phase phenomena in fuel cells. Later, single-phase multi-dimensional models were developed, e.g. Garau et al. [8], Dutta et al. [9,10], Um et al. [11], Mazumder and Cole [12], Meng and Wang [13], and Wang and Wang [14]. Their work is primarily based on the computational fluid dynamics (CFD) approach, where multi-dimensional solutions were obtained by solving transport equations governing conservation of mass, momentum, species, and charge. One major assumption made in several models is to treat the catalyst layers as an interface without thickness. This assumption simplifies fuel cell modeling and facilitates numerical implementation, however may introduce inaccuracy due to neglect

* Tel.: +1 949 824 6004; fax: +1 949 824 8585.
E-mail address: yunw@uci.edu.

0378-7753/$ – see front matter. Published by Elsevier B.V.
doi:10.1016/j.jpowsour.2008.07.007

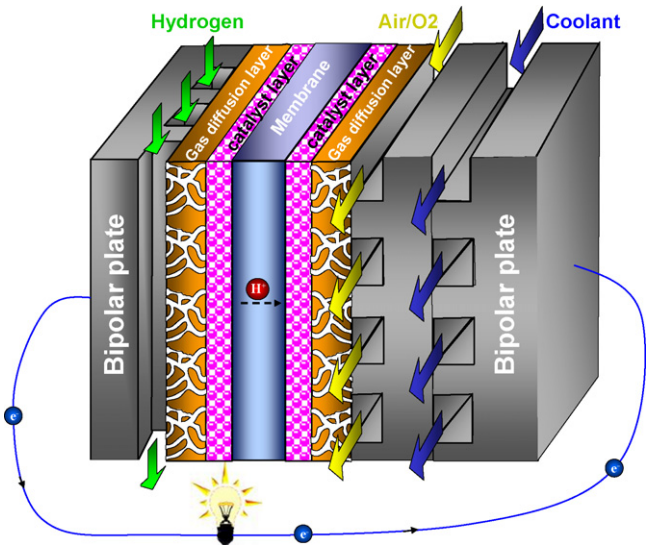

Fig. 1. Schematic of a PEFC.

of electrolyte phase potential variation in the through-plane direction of the catalyst layer. A challenge in fuel cell modeling is multiphase transport in fuel cells. Multiphase flow originates from water production by the oxygen reduction reaction. Liquid water affects gaseous reactant supply and electrochemical catalyst activity. Two-phase modeling have been attempted by He et al. [15], Wang et al. [16], Janssen [17], You and Liu [18], Berning and Djilali [19], Pasaogullari and Wang [20,21] and Weber and Newman [22], which mostly dealt with isothermal conditions. Incorporation of heat transfer has been attempted by Costamagna [23], Mazumder and Cole [24], Birgersson et al. [25], Wang and Wang [26], Weber and Newman [27], and Meng [28]. These previous models mostly focus on steady-state phenomena. Dynamic responses of fuel cells have been investigated by Wang and Wang [29], Hu and Fan [30], Shah et al. [31], Meng [32], and Wang [33].

Though great efforts have been made in PEFC modeling, comprehensive descriptions of fuel cells that elucidate the complex couplings of electrochemical kinetics and multiphase transport are still highly in need. In addition, the majority of previous modeling work only address two-phase flow at high-humidity operations, while the physics of transition from single phase to multiple phases and formation of the evaporation/condensation fronts, are extremely valuable and of paramount importance for fuel cell operation, particularly at low humidity. Further, most of previous studies focus on the cathode flooding, while few include the two-phase flow in the anode. Note that the anode electrode may contribute a major portion of the ionic resistance [29], particularly at low humidity.

In this paper, we seek to develop such a two-phase fuel cell model to elucidate two-phase transports in both anode and cathode diffusion media and their interactions as well as the interactions between single- and two-phase flows and between the two-phase flow and electrochemical reaction. 3D numerical simulations are carried out for a single straight-channel PEFC at low-humidity operation. In particular, we will investigate transition of single-phase flow to multiphase one and formation of the evaporation/condensation front for both co- and counter-flow configurations. Simulation results are presented to reveal distributions of two-phase flow in various parts of the PEFC and validations is made for both low- and high-humidity conditions.

2. Mathematical model

Fig. 1 schematically shows the geometry of a PEFC and the constituent components to be modeled in this work. The two-phase model considers the electrochemical and transport mechanisms in all of the key components including the catalyst layers and membrane. The following assumptions are made: (1) ideal gas mixtures; (2) isotropic and homogeneous membrane, catalyst layers and gas diffusion media; (3) laminar flow due to small pressure gradients and flow velocity; (4) equilibrium between ionomer and surrounding fluid in the catalyst layers; (5) isothermal condition. The model consists of four principles of conservation: mass, momentum, species and charge, and can be presented in concise form as follows:

$$\nabla\cdot\vec{\Gamma}=\vec{S},\quad \text{where}\quad \vec{\Gamma}=\begin{bmatrix}\vec{u}\rho\\ \vec{u}\vec{u}\rho-\vec{\vec{\tau}}\\ \gamma_k\vec{u}C_k+\vec{G}_{k,\mathrm{diff}}\\ \gamma_{\mathrm{w}}\vec{u}C_{\mathrm{w}}+\vec{G}_{\mathrm{w,diff}}+\left(\dfrac{\mathrm{mf}_k^{(\mathrm{l})}}{M_{\mathrm{w}}}-\dfrac{C_k^{(\mathrm{g})}}{\rho^{(\mathrm{g})}}\right)\vec{j}^{(\mathrm{l})}+\vec{G}_{\mathrm{w,perm}}+\dfrac{n_{\mathrm{d}}}{F}\vec{i}^{(\mathrm{m})}\\ -\sigma_{\mathrm{m}}^{\mathrm{eff}}\nabla\Phi^{(\mathrm{m})}\\ -\sigma_{\mathrm{s}}^{\mathrm{eff}}\nabla\Phi^{(\mathrm{s})}\end{bmatrix}$$

$$\text{and}\quad \vec{S}=\begin{bmatrix}0\\ S_u\\ S_{C_k}\\ S_{C_{\mathrm{w}}}\\ S_{\Phi^{(\mathrm{m})}}\\ S_{\Phi^{(\mathrm{s})}}\end{bmatrix} \tag{1}$$

where ρ, $\vec{u}$, p, C_k, C_{w}, $\Phi^{(\mathrm{m})}$, and $\Phi^{(\mathrm{s})}$, denote the multiphase mixture density, superficial fluid velocity vector, pressure, molar concentration of reactant k, water molar concentration, electronic

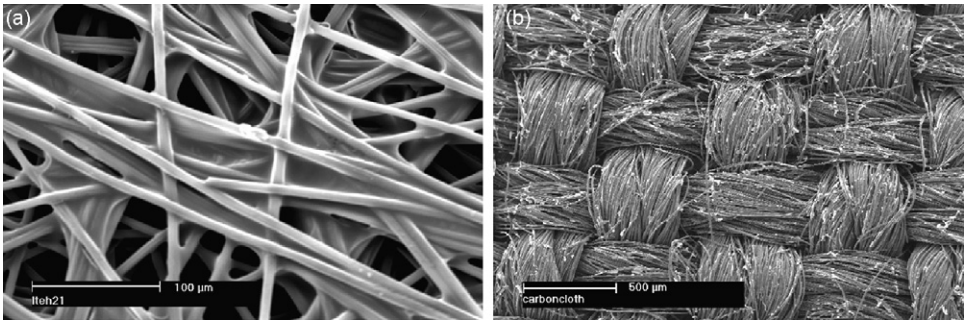

Fig. 2. SEM micrographs of (a) carbon paper and (b) carbon cloth [7].

Table 1
Source terms of the conservation equations in different fuel cell regions

	S_u	S_{C_k}	S_{C_w}	$S_{\Phi^{(m)}}/S_{\Phi^{(s)}}$
Bipolar plates	–	–/–	–/–	–/0
Gas channels	$-\nabla P$	0	0	–
Diffusion media	$-\nabla P - \frac{\mu}{K_{DM}}\vec{u}$	0	0	–/0
Anode catalyst layer	$-\nabla P - \frac{\mu}{K_{CL}}\vec{u}$	$-\frac{j}{2F}$	0	j/$-j$
Cathode catalyst layer	$-\nabla P - \frac{\mu}{K_{CL}}\vec{u}$	$\frac{j}{4F}$	$-\frac{j}{2F}$	j/$-j$
Membrane	–	0	0	0/–

phase potential, and electrolyte phase potential. $\vec{G}_{diff}$ represents the species diffusion flux in gaseous, liquid and solid electrolyte phases, while $\vec{G}_{w,perm}$ denotes the water flux due to hydraulic permeation. The electrochemical and transport processes are coupled together through model parameters such as diffusion coefficients and the source terms, S_u, S_{C_k}, S_{C_w}, $S_{\Phi^{(m)}}$, and $S_{\Phi^{(s)}}$. The expression of these source terms is summarized in Table 1 in detail. For modeling purpose, the pressure gradient term in the momentum equation of Eq. (1) is included in the source term, S_u, to explicitly show the expression of the Darcy's law in the porous diffusion media and catalyst layers. Discussion of these source terms and necessary constitutive relations as well as the key electrochemical/transport mechanisms are elaborated below.

2.1. Electrochemical kinetics

The catalyst layer consists of four components: electrocatalyst, ionomer, carbon, and void space. Platinum and the alloys of platinum and ruthenium are the typical catalyst materials for PEFCs. Currently, Pt loading is around 0.45 mg cm^{-2} and other novel techniques have been reported in the literature to reduce the value to <0.2 mg cm^{-2} [34,35]. The following electrochemical reactions take place at the triple-phase boundary of the catalyst layer:

Hydrogen oxidation reaction (HOR) in the anode:

$$H_2 \rightarrow 2H^+ + 2e^- \tag{2}$$

Oxygen reduction reaction (ORR) in the cathode:

$$O_2 + 4e^- + 4H^+ \rightarrow 2H_2O \tag{3}$$

The electrochemical kinetics of the above two reactions are described by the well-known Butler–Volmer equation:

$$j = ai_0 \left\{ \exp\left(\frac{\alpha_a}{RT} F\eta\right) - \exp\left(-\frac{\alpha_c}{RT} F\eta\right) \right\} \tag{4}$$

where α_a and α_c are anodic and cathodic charge transfer coefficients, respectively. The exchange current density, i_0, is determined by the catalyst electrochemical kinetics, while the surface-to-volume ratio, a, describes the roughness of porous electrodes. The presence of liquid water in the catalyst layer may reduce the reaction area and the following empirical formula is generally adopted to account for the liquid water coverage:

$$a = (1 - s)^{\tau_c} a_0 \tag{5}$$

in which the liquid water saturation, s, is defined as volume fraction of liquid water in the void space.

In PEFCs, HOR is fast, thus yielding a low anode overpotential. Therefore Eq. (4) in the anode can be adequately simplified to a linear kinetic equation. For ORR, sluggish kinetics results in a high cathode overpotential. Thus, the Butler–Volmer equation can be approximated by Tafel kinetics:

$$\text{In the anode}: \quad j_a = ai_{0,a}^{ref} \left(\frac{C_{H_2}}{C_{H_2}^{ref}}\right)^{1/2} \left(\frac{\alpha_a + \alpha_c}{RT} F\eta\right) \tag{6}$$

$$\text{In the cathode}: \quad j_c = -ai_{0,c}^{ref} \left(\frac{C_{O_2}}{C_{O_2}^{ref}}\right) \exp\left(-\frac{\alpha_c F}{RT}\eta\right) \tag{7}$$

where the surface overpotential is defined as

$$\eta = \Phi^{(s)} - \Phi^{(m)} - U_o \tag{8}$$

The equilibrium potential, U_o (V), is zero in the anode, while in the cathode it is a function of temperature [36]:

$$U_o = 1.23 - 0.0009(T - 298) \tag{9}$$

The electrolyte phase potential, $\Phi^{(m)}$, is the driven force for proton movement. The proton conductivity, σ_m, is determined by local membrane water content. In molecular scale, the polymer electrolyte membrane, typically Nafion®, is characterized by hydrophobic, fluorinated main chains with hydrophilic sulfonic acid side chains. The protons are weakly attracted to the SO_3^- group in the hydrated region and are able to travel in the solid electrolyte. The relationship between the ionic conductivity and water content in a Nafion® membrane was experimentally measured by Springer et al. [37]:

$$\sigma_m = (0.5139\lambda - 0.326) \exp\left[1268\left(\frac{1}{303} - \frac{1}{T}\right)\right] \tag{10}$$

where λ denotes the water content in the membrane, defined as the ratio of the number of water molecules to the number of charge ($SO_3^-H^+$) sites. We adopt the following formula to calculate the value of λ [37]:

$$\lambda = \begin{cases} 0.043 + 17.81a - 39.85a^2 + 36.0a^3 & \text{for } 0 < a \le 1 \\ 14 + 8s & \text{for } 0 < s \le 1 \end{cases},$$

$$a = \frac{C_w}{C_{sat}} \text{ and } C_{sat}(T) = \frac{P_{sat}(T)}{RT},$$

$$\text{where} \quad \log_{10} P_{sat} = -2.1794 + 0.02953(T - 273.15) - 9.1837 \times 10^{-5}(T - 273.15)^2 + 1.4454 \times 10^{-7}(T - 273.15)^3 \tag{11}$$

where a denotes the water vapor activity. In catalyst layers or Gore™ membranes, the value of the ionic conduction coefficient is modified according to the Bruggeman relation:

$$\sigma_m^{eff} = \varepsilon_m^{\tau_m} \sigma_m \tag{12}$$

where τ_m is the Bruggeman factor and ε_m denotes the volume fraction of ionomer. In addition, the work of Ma et al. [38] indicates ionic conductivity anisotropy in the membrane. In that case, σ_m^{eff} in Eqs. (10) and (12) can be written in a vector form denoting the conduction coefficient in three dimensions.

Once the electrolyte phase potential is calculated through Eq. (1), the protonic current flux in the membrane can be expressed as

$$\vec{i}^{(m)} = -\sigma_m^{eff} \nabla \Phi^{(m)} \tag{13}$$

Note that $\vec{i}^{(m)}$ is a vector and represents the current flows in three dimensions. To calculate the average current density, one can integrate $\vec{i}^{(m)}$ over a cross-section of the membrane:

$$I = \frac{1}{A_m} \iint_{\text{cross-section}} \vec{i}^{(m)} \cdot d\vec{S} \tag{14}$$

2.2. Multiphase flow

One of the most complex phenomena in PEFCs is multiphase transport, originating from water production by the oxygen reduction reaction. Liquid droplets may block pore paths and hamper the reactant transport to the reaction site, leading to a substantial voltage loss. Following the M2 theory [39], we define the two-phase mixture density as

$$\rho = s\rho^{(l)} + (1-s)\rho^{(g)} \tag{15}$$

where s is the liquid water saturation. In addition, $\rho^{(g)}$ is determined by the constituent species and their contents in the gas, and its values on the anode and cathode sides are quite different. Note that the mixture density is the gaseous density when no liquid water is present. The liquid saturation, s, is obtained from the following relation with the mixture water concentration, C_w, after the latter is solved from the water equation in Eq. (1):

$$s = \begin{cases} 0 & C_w \le C_{sat} \\ \dfrac{C_w - C_{sat}}{\rho^{(l)}/M_w - C_{sat}} & C_w > C_{sat} \end{cases} \tag{16}$$

The interaction of the two phase flows in the diffusion media is described through the relative permeabilities, $k_r^{(l)}$ and $k_r^{(g)}$, defined as the ratio of the intrinsic permeability of liquid and gas phases, respectively, to the total intrinsic permeability of a porous medium. Physically, these parameters describe the extent to which one fluid is hindered by others in pore spaces, and hence can be formulated as a function of liquid saturation. Most of previous work adopted cubic relations. Here, we take the following formula for relative permeabilities [40]:

$$k_r^{(l)} = s^4 \quad \text{and} \quad k_r^{(g)} = (1-s)^4 \tag{17}$$

In pure gas region, s is equal to zero therefore the above multiphase flow equation is back to the single-phase expression.

In addition, the flows may also be affected by the electrochemical activities in the catalyst layers as well as the transport processes between the solid electrolyte and fluid. A mass source term is generally added in Eq. (1) to describe this effect as derived by Wang and Wang [14], who also concluded that the mass source term has negligible impacts on reactant transport and cell performance prediction. Similar assumption of neglecting this source term has been adopted by both single- and two-phase models of fuel cells [7,11,12,20,21,29] with some of them validated experimentally [7,11]. A recent paper has presented a theoretical discussion on this assumption [41] and raised some concerns regarding its validity.

2.3. Reactant and water transport

In gaseous phase, the species of hydrogen, oxygen and water follow similar transport mechanisms. For the traditional design of PEFC flow fields, the convective mass transfer dominates the species transport in gas channels, while diffusion is the major mechanism in porous media. For the interdigitated flow field [42] or the one in Ref. [43], convection can be the dominant mechanism in diffusion media.

2.3.1. Transport in gaseous/liquid phase

The multi-component diffusion in the gaseous phase is described by the Stefan–Maxwell equation. To simplify the expression, the Fick's law is generally used. The diffusion flux, $\vec{G}_{diff}$, and the associated diffusion coefficient in various components of fuel cells can be unified as

$$\vec{G}_{diff} = -D^{(g),eff}\nabla C^{(g)}, \quad \text{where} \quad D^{(g),eff} = \frac{\varepsilon}{\tau}D^{(g)} = \varepsilon^{\tau_d}D^{(g)} \quad \text{and}$$

$$D^{(g)} = D_o\left(\frac{T}{353}\right)^{3/2}\left(\frac{1}{P}\right) \tag{18}$$

Note that the term on the right side of the second equation is also referred to as the Bruggeman relation. In the multiphase region, the liquid attaches on the pores' wall, following the same morphology of the DM solid matrix. Thus, the effective gas diffusion coefficient is modified by

$$D^{(g),eff} = [\varepsilon(1-s)]^{\tau_d}D^{(g)} \tag{19}$$

Liquid flows also affect species transport and the impact is included via the convection corrector factor, γ:

$$\begin{cases} \gamma_k = \dfrac{\rho\lambda^{(g)}}{\rho^{(g)}(1-s)} \\ \gamma_w = \dfrac{\rho}{C_w}\left(\dfrac{\lambda^{(l)}}{M_w} + \dfrac{\lambda^{(g)}}{\rho^{(g)}}C_{sat}\right) \end{cases} \tag{20}$$

where the relative mobilities of individual phases, $\lambda^{(l/g)}$, are

$$\lambda^{(l)} = \frac{k_r^{(l)}/\nu^{(l)}}{(k_r^{(l)}/\nu^{(l)}) + (k_r^{(g)}/\nu^{(g)})}$$

$$\text{and} \quad \lambda^{(g)} = \frac{k_r^{(g)}/\nu^{(g)}}{(k_r^{(l)}/\nu^{(l)}) + (k_r^{(g)}/\nu^{(g)})} \tag{21}$$

Liquid water transport in the diffusion media is driven by the liquid pressure which is calculated by

$$P^{(l)} = P_c + P^{(g)} = \tau\cos(\theta_c)\left(\frac{\varepsilon}{K}\right)^{1/2}J(s) + P^{(g)} \tag{22}$$

where P_c is the capillary pressure and τ is the surface tension. The expression of P_c in the above is called the Leverett function, and $J(s)$ for hydrophobic diffusion media is given by

$$J(s) = 1.417s - 2.120s^2 + 1.263s^3 \tag{23}$$

Note that the Leverett J-function only considers the impact of two characteristics of a porous medium, i.e. porosity and permeability, while ignoring the effect of detailed pore morphology [44]. In addition, diffusion media materials are typically made hydrophobic through adding PTFE to facilitate water removal. The PTFE loading, commonly ranging from 5 to 30%, has significant influence on the contact angle, θ_c. High PTFE loadings have been studied by Lin and Nguyen [45]. Once the capillary pressure is calculated, the flux, $\vec{j}^{(l)}$, in the water equation of Eq. (1) can be obtained through

$$\vec{j}^{(l)} = \frac{\lambda^{(l)}\lambda^{(g)}}{\nu}K[\nabla P_c + (\rho^{(l)} - \rho^{(g)})\vec{g}] \tag{24}$$

Note that the capillary flux term $((mf_k^{(l)}/M_w) - (C_k^{(g)}/\rho^{(g)}))\vec{j}^{(l)}$ in the water equation of Eq. (1) also accounts for the water transport by the gas flow induced by capillary liquid flow [39].

In addition, note that the liquid water transport in the channel may affect the two-phase transport in the diffusion media through the interaction at the interface between the diffusion media and channel. However, at current, few two-phase models have been developed to accurately describe the channel flooding due to its complexity. Therefore, most of previous models [7,20,21,24] including the one in this paper neglect its impacts and assume zero liquid water saturation on diffusion media surface, with focus on the two-phase physics within the diffusion media.

2.3.2. Water transport in the ionomer

Water transport also takes place in the solid electrolyte. Water in the membrane is essential for the ionic conductance, see Eq. (10). Two processes may affect the membrane hydration, one is the water electro-osmotic drag; the other is water back-diffusion. The coefficient of the electro-osmotic drag, n_d, depends on the local water content [46]:

$$n_d = \begin{cases} 1.0 & \text{for } \lambda \le 14 \\ \frac{1.5}{8}(\lambda - 14) + 1.0 & \text{otherwise} \end{cases} \quad (25)$$

The water diffusion coefficient in the membrane is also a function of water content [47] and the diffusive flux is given by

$$\vec{G}_{w,diff} = -D_w^{(m)} \nabla C_w^{(m)} \quad (26)$$

where

$$D_w^{(m)} = \begin{cases} 3.1 \times 10^{-3} \lambda (e^{0.28\lambda} - 1) e^{-2436/T} & \text{for } 0 < \lambda \le 3 \\ 4.17 \times 10^{-4} \lambda (1 + 161\, e^{-\lambda}) e^{-2436/T} & \text{otherwise} \end{cases} \quad (27)$$

As to the catalyst layers or Gore™ membranes, the diffusion coefficient in the portion of the ionomer is modified by

$$D_w^{(m),eff} = \varepsilon_m^{\tau_m} D_w^{(m)} \quad (28)$$

Assuming local microscopic thermodynamic equilibrium between ionomer and surrounding fluid, one can combine the diffusive transport in the void space and ionomer by defining an effective diffusion coefficient:

$$D_w^{eff} = \varepsilon^{\tau_d} D_w^{(g)} + \varepsilon_m^{\tau_m} \frac{\rho^{(m)}}{EW} \frac{RT}{P_{sat}} \frac{d\lambda}{da} D_w^{(m)} \quad (29)$$

where $\rho^{(m)}$ is the density of a dry membrane. Note that by defining thermodynamic equilibrium we combine water transport equations in different phases and there is no need to explicitly express the water exchange rate at the interface in the final form of the equation.

In addition to diffusion, liquid water pressure difference between the two membrane surfaces may lead to hydraulic permeation through the membrane. The permeation flux is determined by the permeability of the membrane, K_m, and liquid pressure gradient:

$$\vec{G}_{w,perm} = -\frac{K_m}{M_w \nu^{(l)}} \nabla P^{(l)} \quad (30)$$

Here, we assume liquid water pressure in the membrane is linear in the thickness direction, determined by the pressures at the membrane surface.

3. Boundary conditions

Eq. (1) form a complete set of governing equations with eight unknowns: $\vec{u}$ (three components), P, C_k, C_w, $\Phi^{(m)}$, and $\Phi^{(s)}$. Their corresponding boundary conditions are described as follows.

3.1. Flow inlet boundaries

The inlet velocity $\vec{u}_{in}$ in a gas channel is expressed by the respective stoichiometric flow ratio, i.e. ξ_a or ξ_c, defined at the average current density, I, as

$$\left(\begin{matrix} \vec{u}_{in,a} \\ \vec{u}_{in,c} \end{matrix} \right) \cdot \vec{n} \Big|_{inlet} = -\frac{IA_m}{F} \left(\begin{matrix} \frac{\xi_a}{2C_{H_2} A_a} \\ \frac{\xi_c}{4C_{O_2} A_c} \end{matrix} \right) \Bigg|_{inlet} \quad (31)$$

where A_a, A_c, and A_m are the flow cross-sectional areas of the anode and cathode gas channels and the membrane area, respectively. The inlet molar concentrations are determined by the inlet pressure and humidity according to the ideal gas law.

3.2. Outlet boundaries

Fully developed or no-flux conditions are applied.

3.2.1. Walls

No-slip and impermeable velocity condition and no-flux condition are applied:

$$\frac{\partial}{\partial n} \left(\begin{matrix} \vec{u} \\ P \\ C_k \\ C_w \\ \Phi^{(m)} \\ \Phi^{(s)} \end{matrix} \right) \Bigg|_{outlet} = 0, \qquad \vec{u}|_{wall} = 0, \quad \text{and}$$

$$\frac{\partial}{\partial n} \left(\begin{matrix} P \\ C_k \\ C_w \\ \Phi^{(m)} \end{matrix} \right) \Bigg|_{wall} = 0 \quad (32)$$

The boundary conditions for the electronic phase potential, $\Phi^{(s)}$, at the bipolar plate outer surfaces can be expressed as

$$\Phi^{(s)}|_{anode} = 0, \qquad \frac{\partial \Phi^{(s)}}{\partial n}|_{cathode} = -\frac{IA_m}{\sigma^{eff} A_{c,wall}}, \quad \text{and}$$

$$\frac{\partial \Phi^{(s)}}{\partial n}|_{otherwise} = 0 \quad (33)$$

where $A_{c,wall}$ is the area of the cathode outer surface.

4. Numerical procedures

The governing equation, Eq. (1), along with their appropriate boundary conditions is discretized by the finite-volume method, with SIMPLE (semi-implicit pressure linked equation) algorithm [48]. For finite-volume discretization, it is convenient to unify all governing equations, including the transient terms, in the following form:

$$\nabla \cdot \vec{\Gamma}(\Theta) = S_\Theta \quad (34)$$

where Θ stands for any dependent variable in Eq. (1). Integrating the above equation throughout an arbitrary volume V bounded by a closed surface S, yields:

$$\oint_S \vec{\Gamma}(\Theta) \cdot d\vec{S} = \int_V S_\Theta \, dv \quad (35)$$

where $\vec{S}$ is the surface vector. Taking V and S to be the volume V_p and discrete faces, S_j, of a computational cell, respectively, one can reach:

$$\sum_j \int_{S_j} \vec{\Gamma}(\Theta) \cdot d\vec{S} = \int_{V_p} S_\Theta \, dv \quad (36)$$

The final form of the discrete finite-volume equation can be expressed as

$$B_p \Theta_p^n = \sum_m B_m \Theta_m^n + B(\Theta_p^0) \quad (37)$$

The above equation is then solved by the algebraic multi-grid (AMG) method.

The mesh of a single-channel PEFC employed here for a numerical study is shown in Fig. 3. About 120,000 ($60 \times 100 \times 12$)

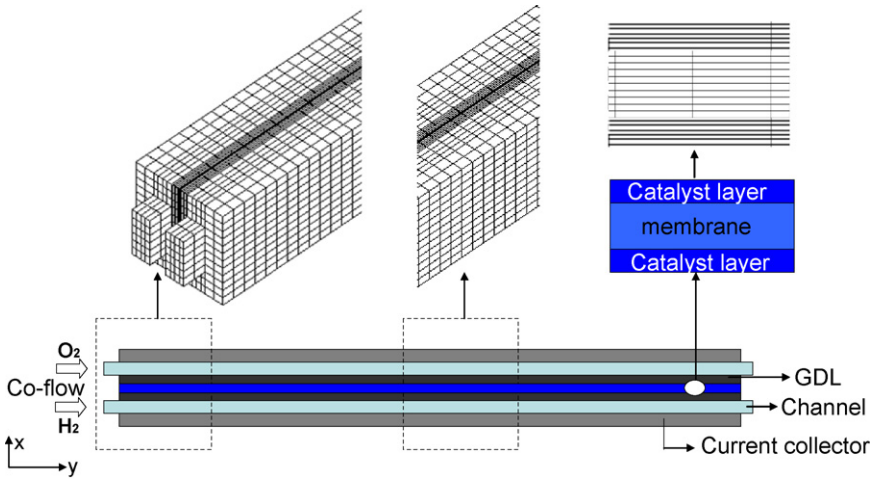

Fig. 3. Computational domain and mesh of a single-channel PEFC.

Table 2
Geometrical, physical, and operating parameters

Quantity	Value
Gas channel depth/width	0.5/1.0 mm
Shoulder width	1.0 mm
GDL/catalyst layer/membrane thickness, δ	0.2/0.01/0.03 mm
Anode/cathode pressures, P	2.0/2.0 atm
Stoichiometry, ξ_a/ξ_c @ 0.8 A cm^{-2}	1.5/2.0
Fuel cell temperature, T	353.15 K
Porosity of GDLs [33]/catalyst layers, ε [40]	0.6/0.4
Volume fraction of ionomer in catalyst layers, ε_m [7]	0.2
Tortuosity, τ_d/τ_m [11]	1.5/1.5
Electronic conductivity of GDLs/bipolar plates, σ_s^{eff} [29]	500/2000 W m^{-1} K^{-1}
Viscosity of liquid water, $\mu^{(l)}$ [20,26]	3.5×10^{-4} kg m^{-1} s^{-1}
Surface tension, liquid–water–air (80 °C), τ [20,26]	0.0625 N m^{-1}
Contact angle, θ_c [7]	110°
Permeability of GDL, K_{DM}/K_m [26]	$10^{-12}/5 \times 10^{-20}$ m^2
Exchange current density × reaction surface area, $a_0 i_{0,a}/a_0 i_{0,c}$ [7]	$1.0 \times 10^9/3.5 \times 10^4$ A m^{-3}
Species diffusivity in anode gas @standard condition, $D_{o,H_2/w}$ [29]	$1.1/1.1 \times 10^{-4}$ m^2 s^{-1}
Species diffusivity in cathode gas @standard condition, $D_{o,O_2/w}$ [29]	$3.24/3.89 \times 10^{-5}$ m^2 s^{-1}

computational cells are used to capture the complex electrochemical and physical phenomena in the PEFC. Geometrical and operating parameters of the PEFC as well as physical properties are listed in Table 2. An average current density is specified as an input parameter, allowing the local current density and electronic phase potential to vary spatially according to local conditions. In all the simulations to be presented in the next section, values of equation residuals are smaller than 10^{-6}.

5. Results and discussion

A single-channel PEFC with the Gore™ 30 μm membrane and carbon cloth diffusion media is chosen for a case study. Both co- and counter-flow configurations of the anode and cathode streams are considered. Air and pure hydrogen are fed in the PEFC. All results are intended to reveal and explore the two-phase phenomena in a PEFC operating at 0.8 A cm^{-2} and inlet humidification of $RH_{a/c}$ = 66/66%. This operation condition indicates typical patterns of two-phase phenomena in both anode and cathode, which are sufficient to demonstrate the fundamentals of two-phase transport within the diffusion media as well as the interaction between anode and cathode two-phase flows in both co- and counter-flow configurations.

Fig. 4 shows contours of the liquid water saturation in the diffusion media under both channel and land. It can be seen that single- and multiphase regions coexist in PEFCs at this low-humidity operation. The single-phase region is near the inlet where the dry gases are fed in. Due to water production by fuel cells, liquid water emerges downstream and the flow in the diffusion media shifts to gas–water multiphase flow. Liquid water emerges first in the cathode side and higher saturation levels appear under the cathode land with the value as high as ~25%. In addition, despite the water electro-osmotic drag, there exists slight flooding in the anode, which may affect the anode electrochemical activity and reactant transport. Anode flooding was also shown in the experiment of Ref. [49]. Further, with the increase of the flow rate in the channel or stoichiometric ratio, the channel stream can remove more water and hence reduce the two-phase region area till liquid disappears. In that case, the present two-phase model changes back to single-phase one and such single-phase phenomena has been addressed adequately in previous literature [12,14,43]. In addition, lowering the external humidification will also diminish the two-phase region.

Fig. 5 shows the reactant concentration contours in the mid-plane of gas channels and diffusion media. It can be seen that oxygen and hydrogen concentrations decrease down the channel

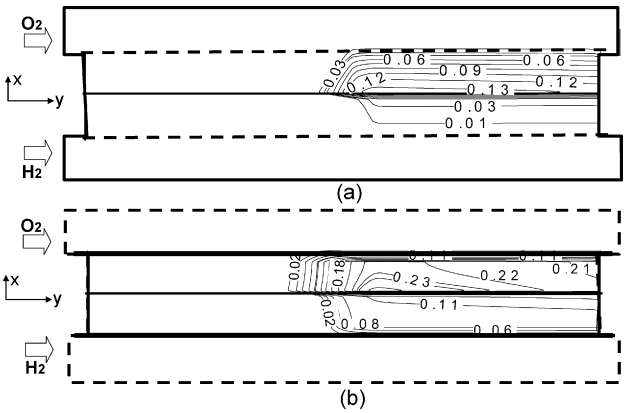

Fig. 4. Liquid water saturation distributions in the diffusion media: (a) under the channel and (b) under the land (operating conditions: $P_{a/c}$ = 2 atm, T_{cell} = 80 °C, $RH_{a/c}$ = 66/66%, and $Stoich._{a/c}$ = 1.5/2).

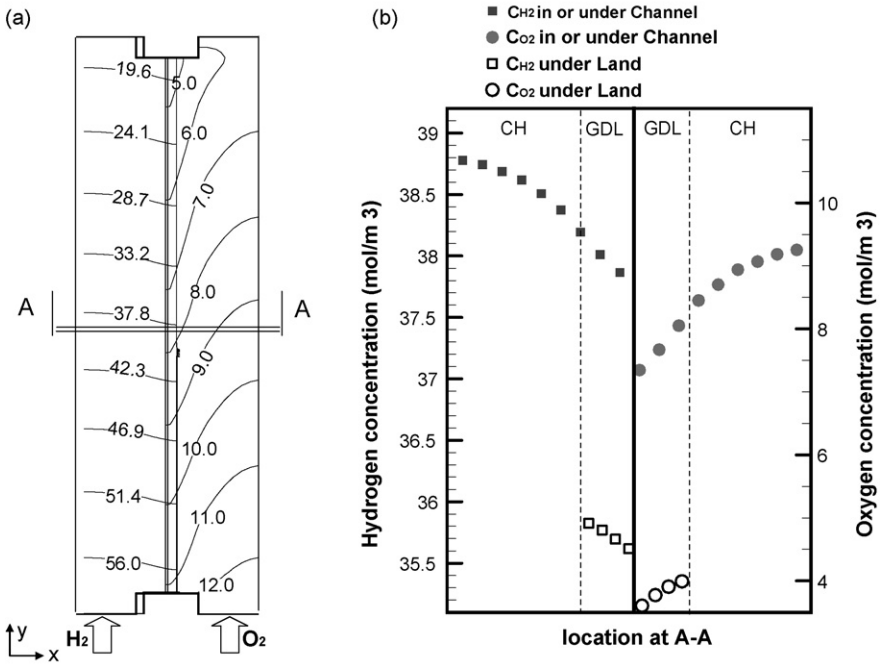

Fig. 5. Reactant profiles of (a) hydrogen and oxygen contours at the middle section of the PEFC and (b) hydrogen and oxygen concentrations under the land and channels at the A–A location (operating conditions: $P_{a/c}$ = 2 atm, T_{cell} = 80 °C, $RH_{a/c}$ = 66/66%, and Stoich.$_{a/c}$ = 1.5/2).

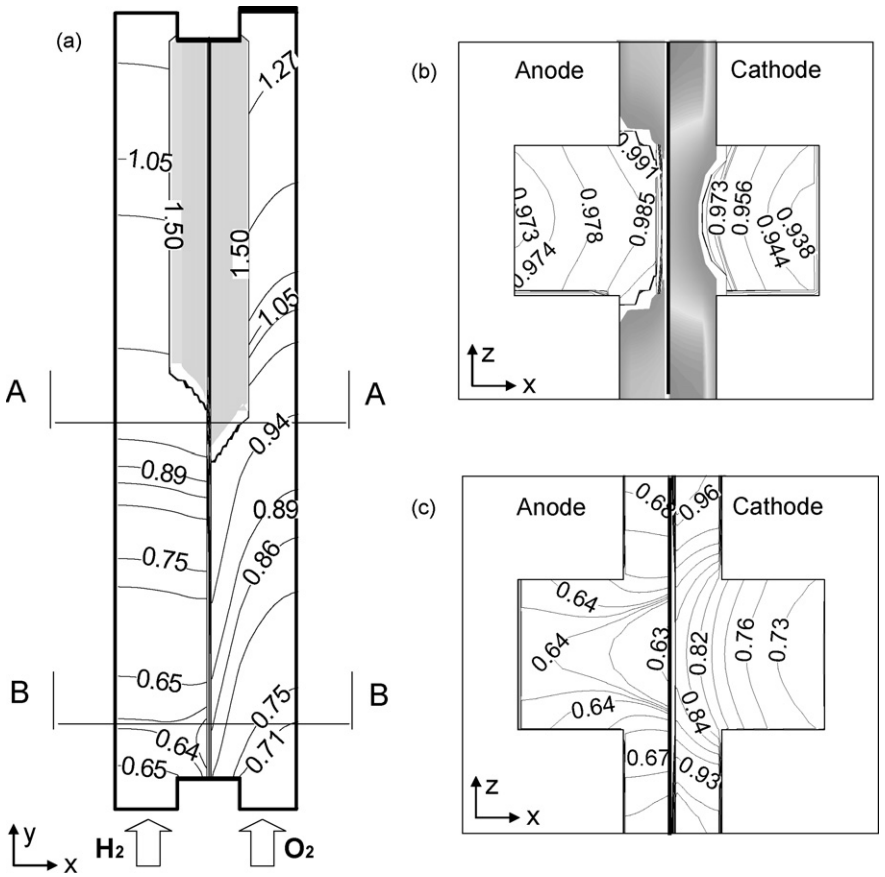

Fig. 6. Relative humidity (RH) distributions: (a) at the middle section of the fuel cell under the channel; (b) at the cross-section of the plane A–A and (c) at the cross-section of the plane B–B. The gray areas denote the multiphase region. Here RH is defined by the same formula as the water activity, a (operating conditions: $P_{a/c}$ = 2 atm, T_{cell} = 80 °C, $RH_{a/c}$ = 66/66%, and Stoich.$_{a/c}$ = 1.5/2).

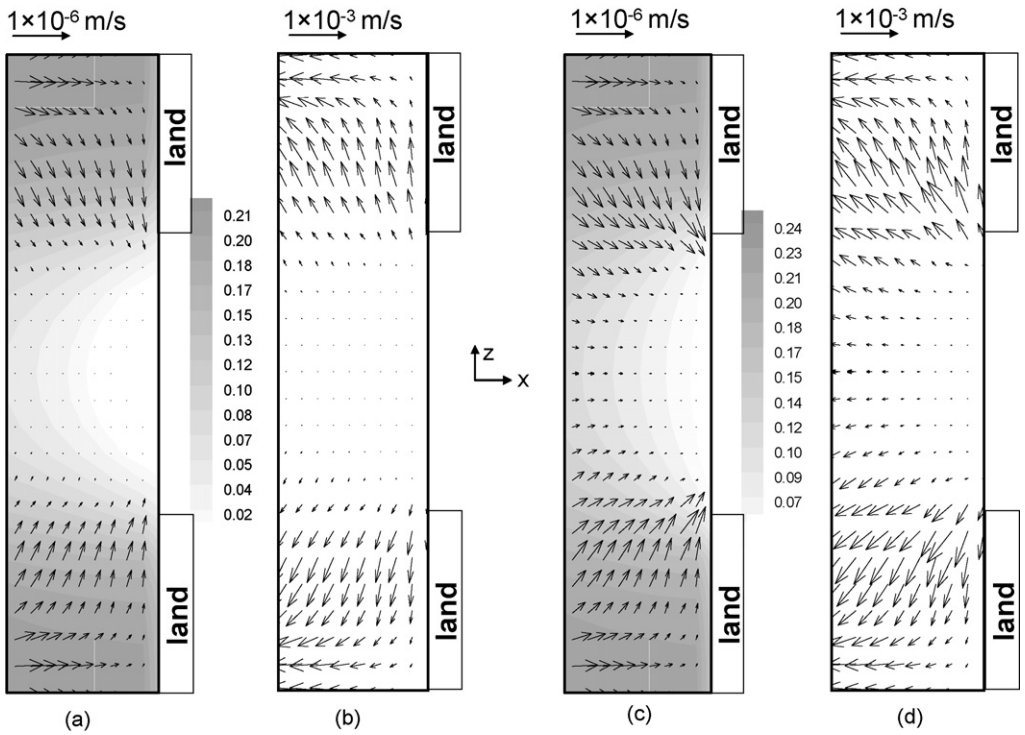

Fig. 7. The velocity and saturation distributions in the cathode GDL: (a) liquid water velocity and saturation at the cross-section of 50% fraction distance from the inlet; (b) gas velocity at the cross-section of 50% fraction distance from the inlet; (c) liquid water velocity and saturation at the cross-section of 90% fraction distance from the inlet; (d) gas velocity at the cross-section of 90% fraction distance from the inlet (operating conditions: $P_{a/c}$ = 2 atm, T_{cell} = 80 °C, $RH_{a/c}$ = 66/66%, and $Stoich._{a/c}$ = 1.5/2).

due to reaction consumption. In contract to the substantial decrease in the along-channel direction, the concentration only experiences a small decline across the GDLs. In addition, the transport resistance under the land is relatively large, leading to a considerable drop in the reactant concentration. As the hydrogen diffusivity is larger than the one of oxygen in the air, the hydrogen profile is more even in the through-plane direction and its concentration undergoes a smaller drop under the land.

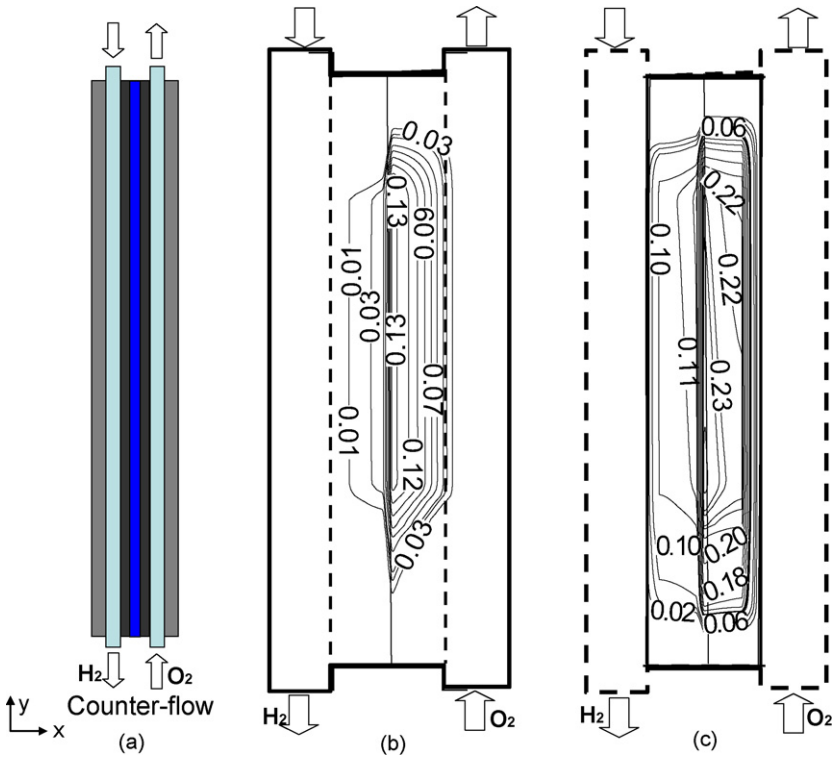

Fig. 8. (a) Schematic of the PEFC with counter-flow configuration, and the contours of liquid water saturation: (b) under the channel and (c) under the land (operating conditions: $P_{a/c}$ = 2 atm, T_{cell} = 80 °C, $RH_{a/c}$ = 66/66%, and $Stoich._{a/c}$ = 1.5/2).

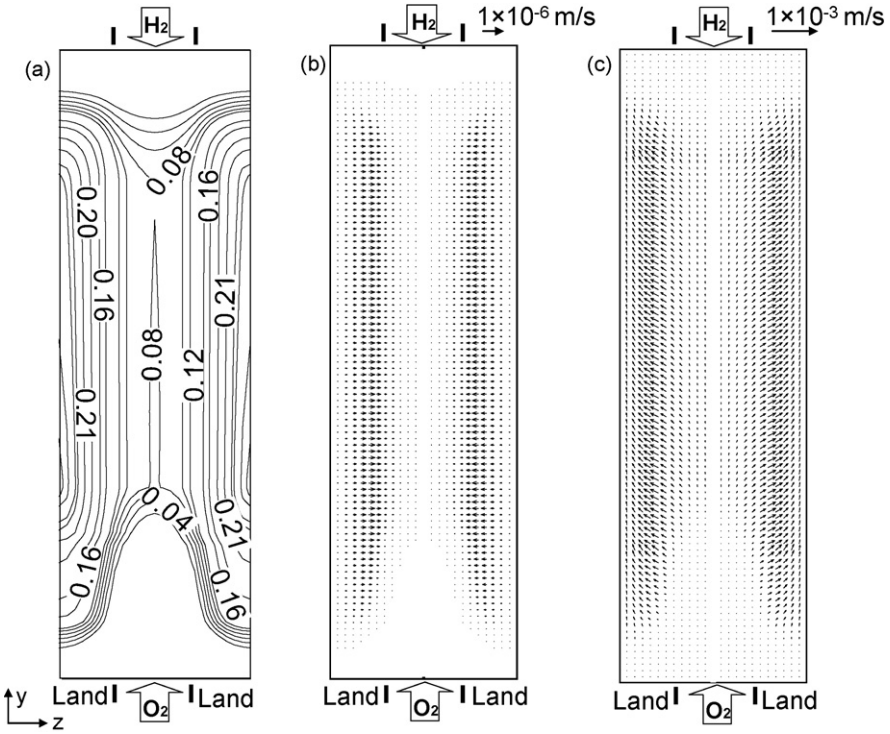

Fig. 9. The distributions of (a) the liquid water saturation, (b) liquid water velocity, and (c) gaseous velocity at middle section of the cathode GDL for the counter-flow (operating conditions: $P_{a/c}$ = 2 atm, T_{cell} = 80 °C, $RH_{a/c}$ = 66/66%, and Stoich.$_{a/c}$ = 1.5/2).

Fig. 6 shows the relative humidity (RH) profiles at different locations of the fuel cell. In Fig. 6(a), the RH in the anode side decreases initially due to the water loss caused by the electro-osmotic drag. It starts increasing as back-diffusion dominates water transport across the membrane. Here, RH is defined by the same formula as the water activity, *a*, in Eq. (11), which considers the water molecules in both liquid and gaseous phases, therefore the RH can be over 1 as shown in the figure. Fig. 6(b) shows the RH distribution at the cross-section of plane A–A, where liquid water emerges. At this location, the anode is subjected to flooding under the land while there is no liquid water under the channel. At the location of B–B, i.e. upstream region, the RH is lower than 1 on both side as shown in Fig. 6(c) and therefore no liquid water appears. In contrast to Fig. 6(b), Fig. 6(c) indicates that the lowest water concentration in the anode is in the diffusion media under the channel, therefore both anode channel and the region under the land supply water to the anode catalyst layer under the channel to compensate for the water loss caused by the electro-osmotic drag. This is partly due to the higher transport resistance under the land, which forces more produced water in the cathode to diffuse back to the anode side under the land.

Fig. 7 shows the velocity and saturation distributions in the cathode GDL at two cross-sections. At the location of 50% fraction distance, there exists slight flood under the channel, therefore the local liquid velocity is quite small as shown in Fig. 7(a). In addition, the liquid flows are uniformly from the catalyst layer to the gas channel and from under-land region to the one under the channel, which shows water removal from the catalyst site. The mass

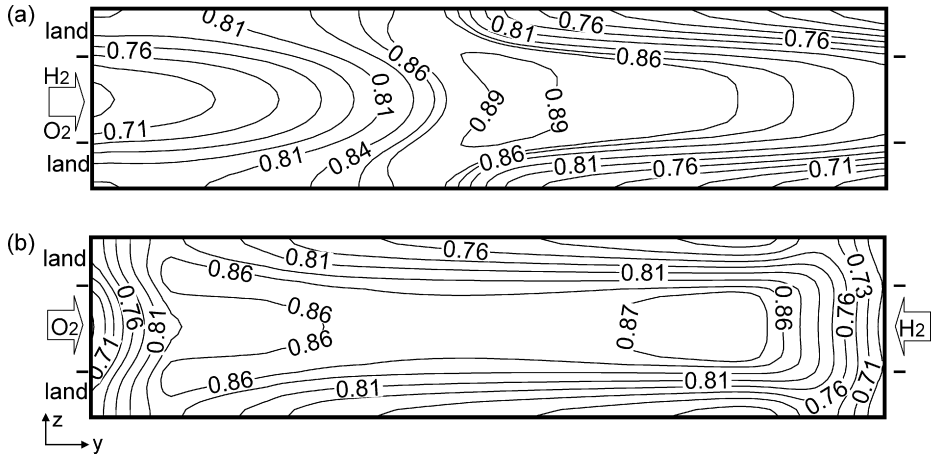

Fig. 10. The contours of protonic current densities at the middle section of the membrane for (a) co-flow and (b) counter-flow cases (operating conditions: $P_{a/c}$ = 2 atm, T_{cell} = 80 °C, $RH_{a/c}$ = 66/66%, and Stoich.$_{a/c}$ = 1.5/2).

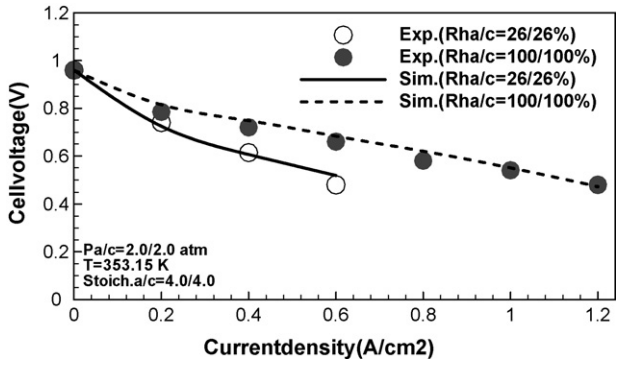

Fig. 11. Polarization curves under both low- and high-humidity conditions. The experimental data are obtained from Ref. [7].

flow of the liquid water is accompanied by a reverse gas flow in the porous media, indicative of the complexity of the multiphase flow phenomena in fuel cells.

Previous results are for the operation of a PEFC with co-flow configuration. Alternative flow field currently under intensive study is counter-flow, i.e. the fuel and air flows are set in opposite directions. Fig. 8(a) shows schematic of a PEFC with such flow field. The idea of the counter-flow design is to humidify the inlet reactant flows through an internal water recirculation and therefore reduce the requirement for external humidification. Fig. 8(b) and (c) present contours of liquid water saturation in the middle section of the under-channel and under-land regions, respectively. In contrast to the ones of co-flow case in Fig. 4, liquid water appears only in the middle of the fuel cell. Similarly, the cathode is subjected to a more severe flooding and liquid water first emerges in the cathode. However, as the cathode outlet is set close to the dry anode inlet region, water is transported to the anode side via the membrane, leading to the transition of cathode two-phase flow back to single-phase one. As the anode wet flow downstream humidifies the dry cathode inlet reactant, liquid water emerges much earlier in the cathode comparing with the co-flow case.

Fig. 9 shows distributions of liquid water saturation, together with velocities of liquid and gas flows, at the middle section of the cathode diffusion media for the counter-flow. It can be seen that the under-land GDL is subjected to more severe flooding and liquid flow is uniformly from the under-land region to the under-channel one where it is taken away by the channel stream. In addition, the channel has a pressure gradient along the channel due to the channel viscous flow, which will affect the gaseous flow in the diffusion media according to the Darcy's law and induce an along-channel component of the gas velocity, as shown in Fig. 9(c).

Fig. 10 shows contours of the current densities at the middle section of the membrane for both co- and counter-flow cases. Both cases show typical distributions of the current density under low-humidity operation, i.e. higher current density appears in the middle of the fuel cell. Near the inlets, dry reactants dehydrate the membrane, leading to a substantial ohmic resistance. As to the co-flow, liquid water near the outlet increases the mass transport polarization, leading to a low local performance downstream. Fig. 11 shows the validation result under both low- and high-humidity conditions. The output voltage is a key parameter inductive of cell performance. The figure shows a good agreement between the model predictions and experimental data.

6. Conclusions

In this paper, a fuel cell model was developed and 3D numerical simulations were carried out to elucidate the fundamentals of complex two-phase transport in both anode and cathode diffusion media and their interactions as well as the interactions between single- and two-phase flows and between two-phase flows and electrochemical reactions. Simulation results revealed detailed two-phase phenomena under low humidity operation for both co- and counter-flow configurations. We found that two-phase flow can occur in both anode and cathode and that at low-humidity operation single- and multiphase flows coexist in a fuel cell. In the co-flow configuration, liquid emerges downstream due to water production by fuel cells, while flooding is more severe in the middle of the fuel cell for the counter-flow configuration due to the internal humidification. In both flow configurations, flooding area under the land is larger than the one under the channel. The voltage predictions of the model agreed well with experimental data. The validated model can be employed for detailed fundamental and parametric studies, such as key parameters governing the anode flooding, impacts of the anode flooding, factors affecting the single- and two-phase regions, and advanced water management, for next generation high performance PEFCs.

Acknowledgements

Partial support of this work by the SETsquared UK US Collaborative Program and the Academic Senate Council on Research, Computing & Library Resources is gratefully acknowledged.

Appendix A. Nomenclature

a	water activity; effective catalyst area per unit volume ($m^2\ m^{-3}$)
a_0	catalyst surface area per unit volume ($m^2\ m^{-3}$)
A	electrode area (m^2)
C	molar concentration of species k ($mol\ m^{-3}$)
D	species diffusivity ($m^2\ s^{-1}$)
EW	equivalent weight of dry membrane ($kg\ mol^{-1}$)
F	Faraday's constant (96,487 C per equivalent)
$\vec{G}$	species diffusion/permeation flux ($mol\ m^{-2}$)
$\vec{i}_e$	superficial current density ($A\ cm^{-2}$)
I	current density ($A\ cm^{-2}$)
j	transfer current density ($A\ cm^{-3}$)
$\vec{j}^{(l)}$	mass flux of liquid phase ($kg\ m^{-2}\ s^{-1}$)
k_r	relative permeability
K	permeability (m^2)
L	length (m)
$mf_k^{(l)}$	mass fraction of species k in liquid phase
M	molecular weight ($kg\ mol^{-1}$)
n	the direction normal to the surface
n_d	electro-osmotic coefficient, H_2O/H^+
P	pressure (Pa)
R	universal gas constant ($8.134\ J\ mol^{-1}\ K^{-1}$)
s	liquid saturation
S	source term
t	time (s)
T	temperature (K)
$\vec{u}$	velocity vector ($m\ s^{-1}$)
U_o	equilibrium potential (V)

Greeks

α	transfer coefficient; net water flux per proton flux
γ_c	correction factor for species convection
δ	thickness (m)
ε	porosity
η	surface overpotential (V)

θ_c	contact angle (°)
Φ	phase potential (V)
λ	membrane water content
$\lambda^{(k)}$	mobility of phase k
ν	kinematic viscosity ($m^2\,s^{-1}$)
ξ	stoichiometric flow ratio
ρ	density ($kg\,m^{-3}$)
σ	electronic or ionic conductivity ($S\,m^{-1}$)
τ	surface tension ($N\,m^{-1}$)
$\vec{\vec{\tau}}$	shear stress ($N\,m^{-2}$)

Superscripts and subscripts

a	anode
c	cathode; capillary
CL	catalyst layer
D	diffusion
DMs	diffusion media
eff	effective value
g	gas phase
GDL	gas diffusion layer
in	inlet
k	species; liquid or gas phase
l	liquid
m	membrane phase
o	gas channel inlet value; reference value
ref	reference value
s	solid
sat	saturate value
w	water

References

[1] M.L. Perry, T.F. Fuller, J. Electrochem. Soc. 149 (2002) S59–S67.
[2] J. Larminie, A. Dicks, Fuel Cell Systems Explained, 2nd ed., John Wiley & Sons, 2003.
[3] C.Y. Wang, Chem. Rev. 104 (2004) 4727–4765.
[4] P. Costamagna, S. Srinivasan, J. Power Sources 102 (2001) 242–252.
[5] P. Costamagna, S. Srinivasan, J. Power Sources 102 (2001) 253–269.
[6] J. Benziger, J. Nehlsen, D. Blackwell, T. Brennan, J. Itescu, J. Membr. Sci. 261 (2005) 98–106.
[7] Y. Wang, C.Y. Wang, K.S. Chen, Electrochim. Acta 52 (2007) 3965–3975.
[8] V. Garau, H. Liu, S. Kakac, AIChE J. 44 (1998) 2410.
[9] S. Dutta, S. Shimpalee, J.W. Van Zee, J. Appl. Electrochem. 30 (2000) 135–146.
[10] S. Dutta, S. Shimpalee, J.W. Van Zee, Int. J. Heat Mass Transfer 44 (2001) 2029.
[11] S. Um, C.Y. Wang, K.S. Chen, J. Electrochem. Soc. 147 (2000) 4485–4493.
[12] S. Mazumder, J.V. Cole, J. Electrochem. Soc. 150 (2003) 1503–1509.
[13] H. Meng, C.Y. Wang, J. Electrochem. Soc. 151 (2004) A358.
[14] Y. Wang, C.Y. Wang, J. Electrochem. Soc. 152 (2005) A445–A453.
[15] W. He, J.S. Yi, T.V. Nguyen, AIChE J. 10 (2000) 2053.
[16] Z.H. Wang, C.Y. Wang, K.S. Chen, J. Power Sources 94 (2001) 40–50.
[17] G.J.M. Janssen, J. Electrochem. Soc. 148 (2001) A1313.
[18] L. You, H. Liu, Int. J. Heat Mass Transfer 45 (2002) 2277–2287.
[19] T. Berning, N. Djilali, J. Electrochem. Soc. 150 (2003) A1598.
[20] U. Pasaogullari, C.Y. Wang, J. Electrochem. Soc. 151 (2004) A399.
[21] U. Pasaogullari, C.Y. Wang, J. Electrochem. Soc. 152 (2005) A380–A390.
[22] A.Z. Weber, J. Newman, J. Electrochem. Soc. 152 (4) (2005) A677–A688.
[23] P. Costamagna, Chem. Eng. Sci. 56 (2001) 323–332.
[24] S. Mazumder, J.V. Cole, J. Electrochem. Soc. 150 (2003) A1510–A1517.
[25] E. Birgersson, M. Noponen, M. Vynnycky, J. Electrochem. Soc. 152 (2005) A1021–A1034.
[26] Y. Wang, C.Y. Wang, J. Electrochem. Soc. 153 (6) (2006) A1193–A1200.
[27] A.Z. Weber, J. Newman, J. Electrochem. Soc. 153 (2006) A2205.
[28] H. Meng, J. Power Sources 168 (2007) 218–228.
[29] Y. Wang, C.Y. Wang, Electrochim. Acta 51 (2006) 3924–3933.
[30] G. Hu, J. Fan, J. Power Sources 165 (2007) 171–184.
[31] A.A. Shah, G.-S. Kim, P.C. Sui, D. Harvey, J. Power Sources 163 (2007) 793–806.
[32] H. Meng, J. Power Sources 171 (2) (2007) 738–746.
[33] Y. Wang, J. Electrochem. Soc. 154 (2007) (2007) B1041–B1048.
[34] M.S. Saha, A.F. Gullá, R.J. Allen, S. Mukerjee, Electrochim. Acta 51 (2006) 4680–4692.
[35] J. Wee, K. Lee, S.H. Kim, J. Power Sources 165 (2007) 667–677.
[36] C. Berger, Handbook of Fuel Cell Technology, Prentice-Hall, Saddle River, NJ, 1968.
[37] T.E. Springer, T.A. Zawodinski, S. Gottesfeld, J. Electrochem. Soc. 138 (1991) 2334–2341.
[38] S. Ma, Z. Siroma, H. Tanaka, J. Electrochem. Soc. 153 (2006) A2274–A2281.
[39] C.Y. Wang, P. Cheng, in: J.P. Hartnett Jr., et al. (Eds.), Advances in Heat Transfer, vol. 30, Academic Press, 1997, pp. 93–196.
[40] Y. Wang, C.Y. Wang, J. Electrochem. Soc. 154 (2007) B636–B643.
[41] V. Gurau, R.V. Edwards, J.A. Mann, T.A. Zawodzinski, Electrochem. Solid-State Lett. 11 (2008) B132–B135.
[42] J.S. Yi, T.V. Nguyen, J. Electrochem. Soc. 146 (1999) 38–45.
[43] Y. Wang, C.Y. Wang, J. Power Sources 147 (2005) 148–161.
[44] F.A.L. Dullien, Porous Media: Fluid Transport and Pore Structure, Academic Press, San Diego, 1992.
[45] G. Lin, T.V. Nguyen, J. Electrochem. Soc. 152 (2005) A1942–A1948.
[46] T.A. Zawodzinski, J. Davey, J. Valerio, S. Gottesfeld, Electrochim. Acta 40 (1995) 297–302.
[47] S. Motupally, A.J. Becker, J.W. Weidner, J. Electrochem. Soc. 147 (2000) 3171–3177.
[48] S.V. Patankar, Numerical Heat Transfer and Fluid Flow, Hemisphere Publishing Corp., New York, 1980.
[49] S. Ge, C.Y. Wang, J. Electrochem. Soc. 154 (2007) B998.